

Multimodal Finger-Shaped Tactile Sensor for Multi-Directional Force and Material Identification

Chengcheng Han, Zhi Cao, Ziyao An, Zhiwei Zhang, Zhong Lin Wang,* and Zhiyi Wu*

Multimodal tactile perception is crucial for advancing human–computer interaction, but real-time multidimensional force detection and material identification remain challenging. Here, a finger-shaped tactile sensor (FTS) based on the triboelectric effect is proposed, capable of multidirectional force sensing and material identification. The FTS is composed of an external material identification section and an internal force sensing section. Three materials are embedded into the surface of the silicone shell in the fingerpad, forming single-electrode sensors for material identification. In the force sensing section, the silicone shell's outer surface is coated with conductive silver paste as a shielding layer. The inner wall has four silicone microneedle arrays and a silicone bump, while five silver electrodes are coated on the internal polylactic acid skeleton. The components connect via interlocking structures near the fingernail, allowing localized contact and separation between the silicone shell and skeleton, enabling force direction detection through signals from the five electrodes. Additionally, the outer sensors achieve 98.33% accuracy in recognizing 12 materials. Furthermore, integrated into a robotic hand, the FTS enables real-time material identification and force detection in an intelligent sorting environment. This research holds great potential for applications in tactile perception for intelligent robotics.

perception is not only a fundamental way for humans to interact with their environment but also a crucial component of intelligent robots' perception of the surrounding world.^[2] With the rapid development of artificial intelligence technology, intelligent robots have been widely applied in various fields such as industry, healthcare, and office settings, gradually taking on increasingly complex tasks.^[3] For these jobs, robot fingers frequently need to have a variety of tactile detecting capabilities similar to those of human fingers. For instance, in the process of intelligent object sorting, robots need not only to identify objects but also to grasp them and place them in the designated locations.^[4] To achieve this goal, one important direction is the development of multimodal tactile sensing technologies, which can provide robots with richer and more accurate sensory capabilities, thereby enhancing their performance in complex tasks.^[5]

Based on this, multimodal tactile sensors utilizing piezoresistive,^[6] capacitive,^[7] piezoelectric,^[8] and triboelectric effects

have been widely studied and have made significant progress.^[9] For example, Yamazaki et al.^[10] designed a fiber-optic-based finger-shaped sensor capable of detecting pressure and vibration with high sensitivity. However, this sensor has certain limitations as it consists of only a single sensing unit, making it difficult to effectively detect the contact position and sliding direction of objects, and thus cannot achieve triaxial force sensing. Xu et al.^[11] designed a soft electromagnetic induction-based finger-shaped sensor, which changes the relative position of a coil and magnet under force to enable multidirectional sensing, but the output voltage signal is relatively weak. Sun et al.^[12] developed a 3D force sensor based on cameras and other devices, combined with neural networks to create a 3D force map; however, the device has a relatively complex structure. Tomo et al.^[13] used the Hall effect principle and designed a finger-shaped tactile sensor with 24 Hall sensors, which detects changes in the magnetic field around the array sensors due to applied forces, enabling 3D force sensing and temperature recognition. However, due to its sensing principle, this sensor is susceptible to interference from external magnetic fields. Among these technologies, triboelectric nanogenerators (TENGs) have gained widespread attention due to their ability to directly convert mechanical motion into electrical energy, as well as their advantages such as diverse material selection,

1. Introduction

In nature, humans perceive pressure, temperature, and material properties by extending their fingers to touch objects, which highlights the importance of fingertip tactile sensing.^[1] Tactile

C. Han, Z. Cao, Z. Zhang, Z. L. Wang, Z. Wu
 Beijing Institute of Nanoenergy and Nanosystems
 Chinese Academy of Sciences
 Beijing 101400, China
 E-mail: zhong.wang@mse.gatech.edu; wuzhiyi@binn.cas.cn

C. Han, Z. Cao, Z. Zhang, Z. L. Wang, Z. Wu
 School of Nanoscience and Technology
 University of Chinese Academy of Sciences
 Beijing 100049, P. R. China

Z. An
 The Experimental School of Shenzhen Institute of Advanced Technology
 Shenzhen 51800, P. R. China

Z. Wu
 International Institute for Interdisciplinary and Frontiers
 Beihang University
 Beijing 100191, P. R. China

 The ORCID identification number(s) for the author(s) of this article can be found under <https://doi.org/10.1002/adma.202414096>

DOI: 10.1002/adma.202414096

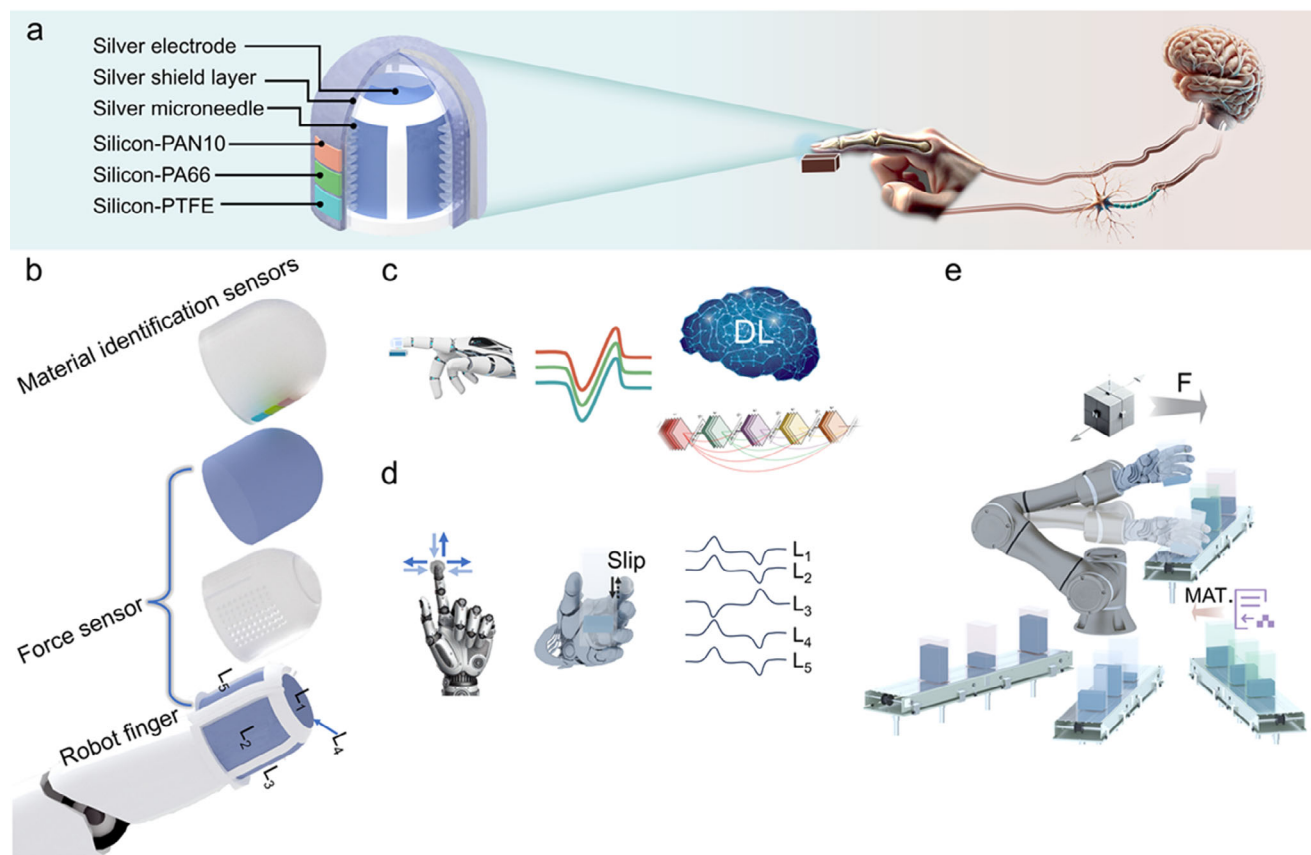


Figure 1. a) Schematic of the overall structure of the FTS inspired by human fingers. b) Schematic diagram of the FTS on a robot and the unfolding of each layer. c) Demonstration of the material identification function in FTS. d) Demonstration of the force sensor function in FTS. e) FTS is applied to material identification and object sorting in an intelligent workshop.

high voltage signals, high sensitivity, and simple manufacturing processes.^[14] As a result, TENG-based multimodal tactile sensors have become a research hotspot. For instance, Zhao et al.^[15] proposed a multilayer-structured triboelectric multimodal tactile sensor (TMTS) capable of simultaneously recognizing different materials, curvatures, and pressures, thereby achieving more accurate detection. However, this sensor can currently only detect force in a single direction.

Here, we propose a finger-shaped tactile sensor (FTS) that can detect multi-directional forces and recognize materials. The FTS consists mainly of an external material recognition section and an internal force sensing section. Like human fingerprint-based material recognition, we embed three different materials into the fingertip area of a silicone shell, forming three single-electrode triboelectric sensors. When the FTS contacts an external object, these sensors interact directly with the object, generating voltage signals related to the contact material. After preprocessing, these signals are input into the ResNet50 deep learning model for feature extraction and analysis, enabling accurate object recognition. Additionally, the micro-needle array and hemispherical protrusions on the inner wall of the silicone shell interact with the silver-plated surface of the polylactic acid (PLA) rigid skeleton, generating friction and relative motion. This interaction causes localized contact and separation, resulting in different voltage signals on five silver electrodes. To ensure the stability of the triboelectric

signals, the outer surface of the micro-needles is silver-plated, effectively shielding against external electrostatic interference.^[16] By analyzing the voltage signals from these five electrodes, the magnitude and direction of the applied force can be precisely determined. We integrate the FTS into a robotic hand to simulate material sorting tasks in a smart workshop. This sensor structure can effectively recognize and grasp objects of certain weights, delivering them precisely to designated locations.

2. Results and Discussion

2.1. Working Principles of the Multimodal Finger-Shaped Tactile Sensor

Inspired by the anatomical structure of the human finger, we introduce a FTS, engineered to detect multidirectional shear and normal forces, emulating the functional capabilities of a human finger. Furthermore, the FTS's silicone surface is embedded with three distinct materials, enabling it to effectively recognize different material types. The detailed structural schematic is illustrated in **Figure 1a**. The device is composed of an innermost PLA rigid frame and an external silicone microneedle soft shell. The innermost PLA framework is coated with five discrete silver electrode layers, with precise dimensions provided in **Figure S1** (Supporting Information). The outer layer, featuring a

conical microneedle structure, is fabricated from silicone with detailed dimensions available in Figure S2 (Supporting Information), and is encased in an external shielding layer formed by a conductive silver coating. These components collectively constitute the force-sensing module of the FTS. The outermost layer, composed of three distinct silicon material-based sensors integrated within the silicone soft shell, serves as the material identification module. The comprehensive fabrication process and actual images of the FTS are provided in Figure S3 (Supporting Information). Figure 1b shows the installation position of the FTS on the robotic hand and a schematic diagram of each layer's structure. The side electrodes, L_1 – L_4 , are symmetrically distributed around the cylindrical surface, while the L_5 electrode is positioned at the top. Importantly, slots for securing the outer shell are designed in the gaps between the L_1 , L_2 , and L_4 electrodes on the rigid internal framework. These slots serve to fix the silicone soft shell in place and act as a support platform for the silicone shell in Figure S4 (Supporting Information). These force-sensing and material identification modules are integrated to form the novel FTS presented in this work. This innovative structural design endows the device with the capability to detect forces in multiple directions while accurately recognizing different material types.

Next, as illustrated in Figure 1c, when the FTS touches different objects, the three single-electrode mode TENGs on the surface generate distinct voltage signals. After preprocessing these waveforms and inputting them into a deep learning model for training, the model can accurately recognize the materials touched by the FTS. Additionally, Figure 1d demonstrates the application of the FTS in directional sensing. When the robot hand's finger equipped with the FTS touches an object and moves back and forth or side to side, the five electrodes generate different voltage waveforms depending on the direction of finger movement and the pressure applied. By analyzing these five voltage waveforms, we can determine the direction and magnitude of the force exerted on the finger. And Figure 1e illustrates the application of the FTS in an intelligent sorting workshop. Here, objects are placed in containers made of different materials, and FTS is mounted on the robotic hand's finger. When the robotic hand's finger touches the objects, the FTS effectively identifies the material of object. Combined with the force sensor in the FTS to detect and feedback on the magnitude and direction of the force, the robotic hand can successfully grasp the objects and move them to the designated conveyor belt. This enables the robotic hand to intelligently recognize and sort different materials efficiently.

In our FTS device, as illustrated in the initial state in Figure 2a, the working principle of the force-sensing component is based on combination of triboelectrification and electrostatic induction, and could be divided into four steps: when the silicone finger is not in contact with an object, the silicone microneedles and silver electrodes maintain a certain distance, and the charge is in an electrostatic equilibrium state, as shown in (I). When the silicone finger encounters the object, the contact force causes the negatively charged silicone microneedles to move closer to the silver electrodes, redistributing the charge and causing electrons to flow from the silver electrode to the ground, making the electrode positively charged (II). When the pressure reaches its maximum, the silicone microneedles further contact the silver elec-

trode, storing elastic potential energy and allowing more electrons to flow to the ground, making the silver electrode more positively charged (III). Subsequently, as the silicone finger separates from the object, the contact force decreases, and the silicone microneedles release their elastic potential energy, moving away from the silver electrode. This separation reduces the induced positive charge on the silver electrode, causing the direction of the current to reverse compared to when contact was made (IV). Finally, the silicone finger returns to its initial state (I), completing a full cycle.

Through simulations, we modeled the deformation of the silicone microneedles under different levels of applied pressure, as shown in Figure 2b, and the detailed video is shown in Video S1 (Supporting Information). It can be observed that as the force applied to the silicone microneedles increases, the deformation of the microneedles becomes more pronounced. Additionally, as the deformation of the microneedles increases, the induced potential on the electrode surface also increases, as shown in the potential distribution in Figure 2c.

Next, as shown in Figure 2d, to enhance the voltage output generated by friction between the silver electrodes and the silicone at a fixed distance, we analyzed the impact of different silicone micro-needle shapes on the output while maintaining the same surface area. The actual images are provided in Figure S5 (Supporting Information), and the corresponding open-circuit voltage (V_{oc}) results are shown in Figure 2e. From the trend of the curves, it can be concluded that the voltage generated by different microneedle structures increases with increasing force. Among them, when the same force is applied, narrower microneedle protrusions generate higher V_{oc} ; therefore, we selected silicone protrusions with a width of 0.5 mm for subsequent experiments. Additionally, we further investigated the output performance of different types of silicone, with the V_{oc} shown in Figure 2f. The results indicate that silicone with a hardness rating of 25 produced the highest V_{oc} , so we chose this silicone type for subsequent device fabrication.

More importantly, considering that the external material and the surface of the silicone shell may also generate triboelectric effects during pressing and separation, leading to potential changes in the internal electrodes, we conducted simulation analyses of the potential variation in the electrodes with and without a shielding layer on the force sensor shell when exposed to charged objects (Figure 2g,h). Specifically, the potential variation of the internal electrodes at different distances, with and without the shielding layer, is shown in Figure 2i. From the trend of the curves, it can be concluded that with the shielding layer, the potential changes caused by the position of the external charged object are significantly smaller compared to those without the shielding layer. The actual images of the designed shielding layer are provided in Figure S6 (Supporting Information). The test setup is illustrated in Figure 2j, where a charged object oscillated back and forth with a peak amplitude stabilized at 2 cm. By increasing the distance between the lowest position of the object's oscillation and the top of the FTS, we measured the V_{oc} variation of top electrode at the FTS's head with and without the shielding layer. The V_{oc} results are shown in Figure 2k, revealing that as the charged object (FEP) moves further away from the FTS, the interference decreases, and the interference with the shielding layer is significantly less than that without the shielding layer. Finally,

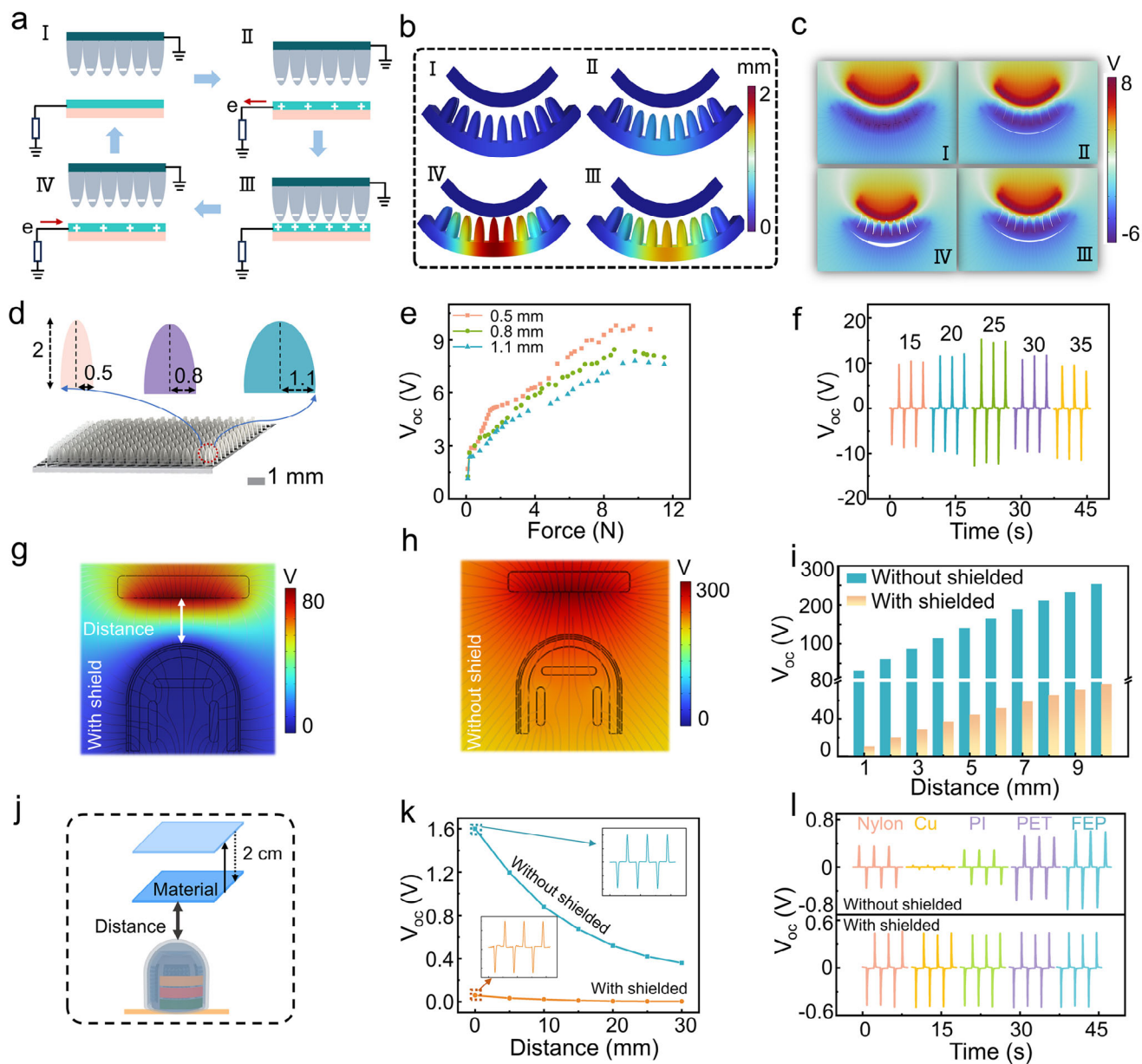


Figure 2. a) Schematic diagram of charge transfer in the force sensor section in FTS. b) Simulation of microstructure displacement variation. c) Simulation of displacement-induced potential variation. d, e) Schematic of different microneedle structures inside the force sensor and corresponding output. f) The V_{oc} of silicone microneedles with different models of silicone. g) Simulated potential distribution with shielding layer. h) Simulated potential distribution without shielding layer. i) Simulated data with and without the shielding layer. j) Experimental test setup at a fixed distance with and without the shielding layer. k) The V_{oc} at different distances with and without the shielding layer. l) The V_{oc} under the same force with different materials, with and without the shielding layer.

we tested the V_{oc} of the FTS with and without the shielding layer under the same pressure applied by different materials. The corresponding V_{oc} waveforms are shown in Figure 2l. The results demonstrate that without the shielding layer, the electrode output varies with changes in the external material, and the V_{oc} generated by the compression and rebound of the silicone are also affected by the external material. Under the same force, the V_{oc} amplitude generated by pressing the FTS with different materials is minimally affected when the shielding layer is present, and the peak and trough sequences of the V_{oc} remain consistent. In

summary, the introduction of the shielding layer structure provides crucial support for the stability of the FTS's output.

Next, we conducted tests on the device by applying normal forces in different directions. As shown in Figure 3a, the left image illustrates the direction of the normal force applied to the FTS and the corresponding distribution of the electrodes. The angle between the force (F) and the Z-axis is denoted as φ , with the Z-axis component represented as F_z , and the component in the XY-plane represented as F_{xy} . The right image shows the positions of the five electrodes on the FTS: electrode L_1 is located directly

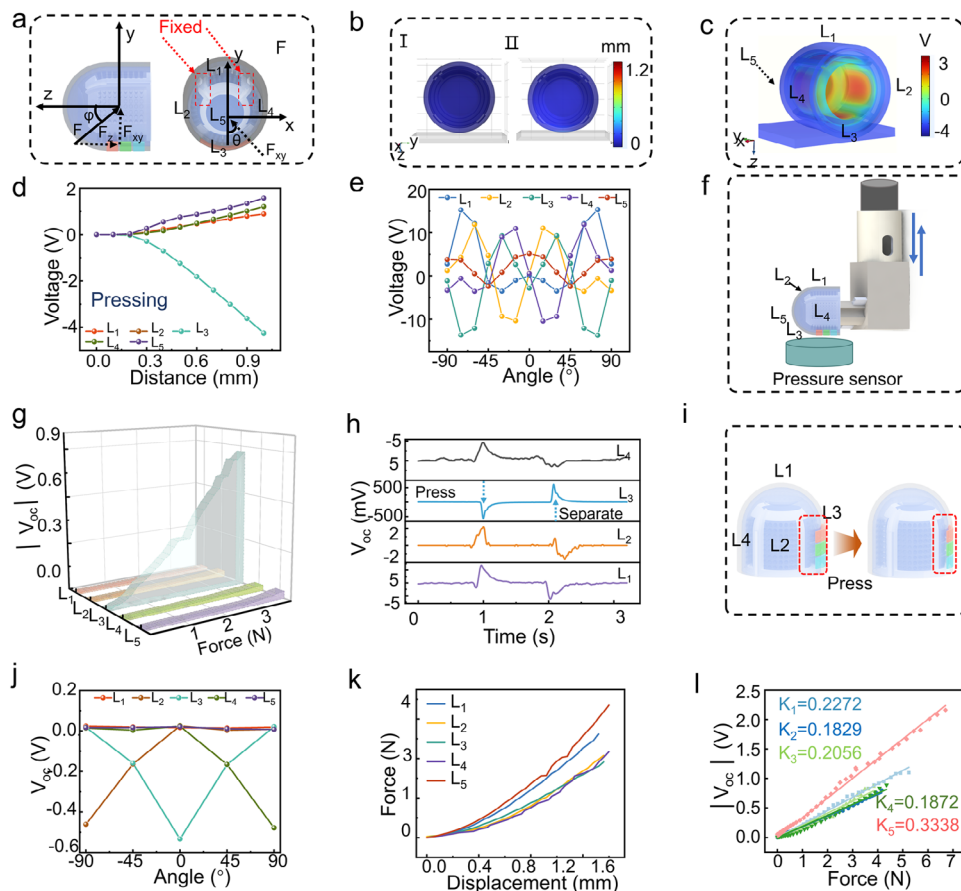


Figure 3. a) Schematic diagram of the normal force angle and electrode positions. b) Deformation of the FTS when a flat object presses in the direction of electrode L_3 . c) Potential distribution when a flat object presses in the direction of electrode L_3 . d) Voltage of the five electrodes as the distance increases when a flat object presses in the direction of electrode L_3 . e) Simulated potential distribution when the flat object compresses the silicone at different θ angles. f) Schematic diagram of the experimental setup for normal force testing. g) $|V_{oc}|$ of the five electrodes under different normal forces with $\theta = 0^\circ$. h) Voltage waveform of electrode L_3 under a normal force of 2 N with $\theta = 0^\circ$. i) Deformation schematic of electrode L_3 under compression. j) Peak-to-peak electrode voltage under different θ angles when pressed. k) Relationship between displacement and force at different electrode positions under normal force. l) $|V_{oc}|$ corresponding to different normal forces for the five electrodes.

above the Y-axis, with the other electrodes labeled L_2 , L_3 , and L_4 in a counterclockwise direction, and electrode L_5 positioned directly above the Z-axis. The angle between F_{xy} and the Y-axis is denoted as θ . To systematically understand the response of the FTS under different normal forces, we performed solid mechanics and electrostatics simulations. In the solid mechanics simulations, a rigid plate at the bottom was moved by a specified displacement to generate the corresponding normal force on the FTS, allowing us to analyze the deformation and force distribution.

In the electrostatics simulations, equal positive charge densities were applied to the five electrodes, and corresponding equal negative charges were applied to the electrode surfaces to analyze the potential variations. Figure 3b shows the deformation of the FTS when a normal force is applied with $\varphi = 90^\circ$ and $\theta = 0^\circ$, with the force applied in the direction of electrode L_3 . The left image depicts the FTS in its undeformed state, where the spacing between the four electrodes and the outer shell is relatively uniform. The right image shows the deformed state of the FTS under external compression, where the gap between electrode L_3 and the outer shell decreases, while electrodes L_2 and L_4 sepa-

rate from the shell, and the detailed video is shown in Video S2 (Supporting Information). Figure 3c displays the corresponding potential distribution under this condition, showing a decrease in the potential of L_3 and an increase in the potential of L_2 and L_4 . Figure 3d summarizes the potential variation of the five electrodes when $\theta = 0^\circ$. Specifically, during the compression process, the potential of electrode L_3 decreases, while the potential of the other electrodes changes in the opposite direction, with L_3 showing the most significant variation. The detailed simulation curves of the voltage changes for each electrode during normal pressing are provided in Figures S7, S8 (Supporting Information). Subsequently, we also analyzed the simulation curves for compression of the FTS at different angles θ , as shown in Figures S9, S10 (Supporting Information), with the corresponding potential differences plotted in Figure 3e. It can be observed that during the angular variation from -90° to 90° , there is a certain symmetry between electrodes L_2 and L_4 , and electrode L_3 exhibits symmetry with respect to the Y-axis.

Subsequently, we conducted corresponding experimental tests, with the experimental setup shown in Figure 3f. The FTS

was mounted on a linear motor via a bracket, with the contacted material positioned at the bottom. A pressure sensor was installed beneath the contact material to measure the magnitude of the contact force. Additionally, by adjusting the reciprocating movement distance of the linear motor, we could control the magnitude of the normal force between the FTS and the test object. By rotating the FTS, we tested the V_{oc} of the different electrodes under various force directions (θ). First, we tested the V_{oc} of the five electrodes at different force magnitudes when θ was set to 0. The absolute values of the V_{oc} are shown in Figure 3g. It can be observed that as the normal force increases, the $|V_{oc}|$ of all electrodes increases accordingly, with the L_3 electrode showing a particularly significant change, while the other electrodes exhibit less noticeable changes. This is mainly due to the more pronounced deformation at the contact position of the L_3 electrode during compression, while other electrodes experienced less deformation. And the triboelectric effect is more significant at the L_3 contact point compared to other positions. In more detail, we measured the waveforms during the contact and separation between the FTS and the object, as shown in Figure 3h. When the FTS contacts the object, the V_{oc} of L_3 shows a negative peak, while the other electrodes exhibit positive peaks, consistent with the simulated potential changes during contact. Upon separation, the L_3 electrode shows a positive peak, while the other electrodes display negative peaks. This behavior is explained by the fact that when the L_3 shell position is pressed, the L_3 electrode encounters the shell, while other positions experience separation, as illustrated in Figure 3i. Subsequently, we applied a 3 N normal force at different θ angles and measured the V_{oc} of the electrodes, with the summarized results shown in Figure 3j. During the angle change from -90° to 0° , the V_{oc} of the L_2 and L_3 electrodes changes significantly. The absolute value of the L_2 electrode voltage decreases as the angle increases, while the absolute value of the L_3 electrode voltage increases with the angle. Conversely, as θ changes from 0° to 90° , the absolute value of the L_3 electrode voltage decreases with increasing angle, while the absolute value of the L_4 electrode voltage increases. These findings indicate that the direction of the tangential force can be determined by analyzing the relationships between the absolute values and the polarity of the electrode voltages. As shown in Figure 3k, we tested the relationship between displacement and force at different electrode positions under normal pressure. It can be observed that as the displacement increases, the force also increases. The change patterns for L_2 , L_3 , and L_4 are similar, while the change rates for L_1 and L_5 are relatively larger. This can be attributed to the structure of the FTS: L_1 has a fixed ridge structure at its position, and the contact area of the L_5 electrode is relatively large. Based on this, we plotted the absolute V_{oc} of the corresponding voltages under different normal forces in Figure 3l. There is a good linear relationship between the absolute value of the electrode V_{oc} and the applied force. Consequently, the normal force can be calculated by analyzing the electrode voltages.

We conducted a series of analyses and tests on the FTS's response to shear forces. During the simulation process, we first moved the object upwards and then horizontally, simulating the state changes as the FTS slides to the left, as illustrated in Figure 4a. I) The initial positions of the object and the FTS are shown; II) After the object has moved upwards, significant deformation can be observed at the position of electrode L_3 ; III)

After the object moves horizontally, separation occurs between electrode L_2 and the outer shell along the direction of the object's movement, while compression occurs at electrode L_3 . And Figure 4b shows the potential changes of the five electrodes. During the upward movement, the potential of electrode L_3 decreases while the potential of the other electrodes increases, consistent with the behavior observed during normal force compression. Subsequently, as the object moves horizontally, the potentials of electrodes L_2 and L_4 exhibit significant changes, with the trends of these changes being opposite to each other. The dynamic process of the above simulation is shown in Video S3 (Supporting Information).

Then, we conducted experimental tests on the FTS's response to shear forces, as illustrated in the schematic diagram in Figure 4c. The FTS was tested by moving it front and back, left, and right. The corresponding experimental setup is shown in Figure S11 (Supporting Information). Figure 4d presents the relationship between displacement and force during the front and back movement of the FTS under different normal pressures. It can be observed that as the normal force increases, the shear force on FTS also increases for the same displacement. When the normal force is fixed, the shear force initially increases with displacement and then tends to stabilize. During the experiments, it was observed that with small displacements, the FTS's internal twisting occurs, with minimal displacement between the FTS and the object.

Once the displacement exceeds a certain threshold, sliding occurs between the FTS and the object. The relationship between displacement and force during left and right movements is shown in Figure S12 (Supporting Information). Figure 4e illustrates the $|V_{oc}|$ of the five electrodes under different shear forces with a normal pressure of 2 N. During forward movement, the outputs of electrodes L_5 and L_3 are significantly higher, while the other electrodes exhibit relatively minor changes. The corresponding voltage waveforms during forward movement are shown in Figure 4f, where electrodes L_5 and L_3 display similar trends with much higher magnitudes compared to the other electrodes. Figure 4g shows the V_{oc} waveforms during left and right movements. During leftward movement, electrodes L_2 , L_3 , and L_4 exhibit the most significant changes, with electrode L_2 showing a positive-to-negative transition, while electrode L_4 shows a negative-to-positive transition, indicating opposite trends. Similarly, during the rightward movement, these three electrodes again play a major role, but in this case, electrode L_2 shows a negative-to-positive trend, while electrode L_4 shows a positive-to-negative trend.

Through these tests, we systematically explored the FTS's output under shear forces of varying magnitudes and directions. The V_{oc} from the five electrodes provide a reliable basis for determining the direction of movement of the FTS. This structural design lays a solid foundation for accurate recognition of shear force directions.

2.2. Resnet50-Assisted Tactile Sensing System for Material Identification

With the aid of our FTS device, future robots may be able to achieve effective sensing capabilities that are beyond human

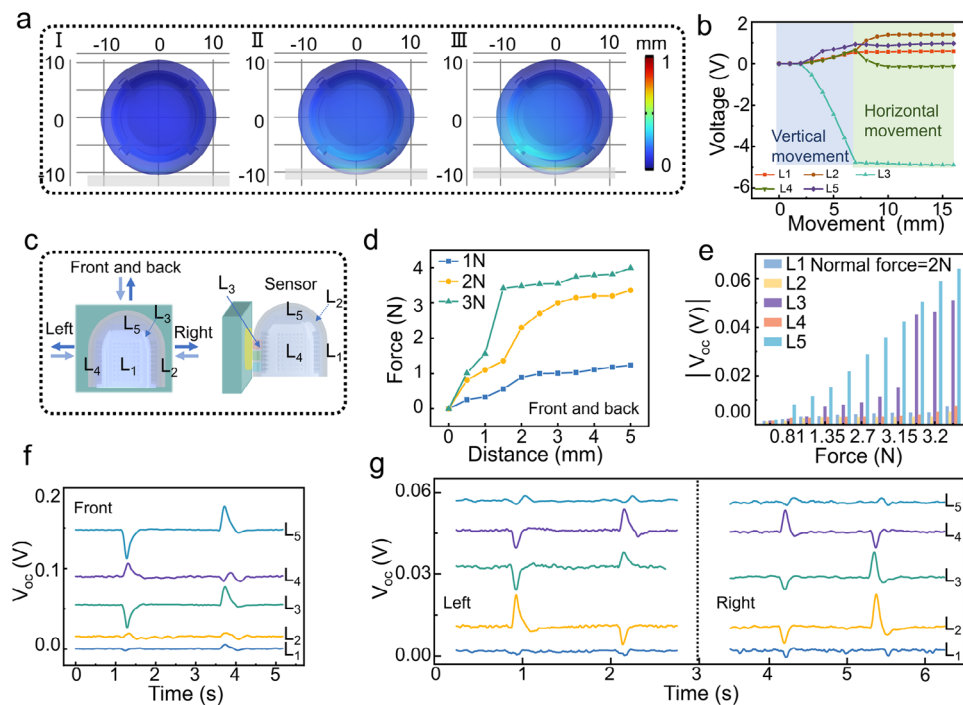


Figure 4. a) Simulation of the shear force process on the FTS: I. Initial state; II. State after upward movement of the flat plate; III. State after horizontal movement of the FTS. b) Potential curves of the five electrodes during the simulation process. c) Schematic diagram of the experimental setup for shear force testing. d) Relationship between displacement and force during forward movement of the FTS under different normal pressures. e) Peak-to-peak voltage values of the five electrodes under different shear forces with a normal pressure of 2 N. f) V_{oc} of the five electrodes during forward movement. g) V_{oc} waveforms during leftward and rightward movement of the object.

touch. **Figure 5a.** illustrates the complete process from signal acquisition to data processing through deep learning. One of the key challenges in deep learning is finding an effective method to identify and extract features during the complex input signal classification steps from seemingly independent datasets. In this experimental setup, the composition and the distribution of the three-material identification in FTS are shown in **Figure 5b**. The three sensors are made of silicone-Polyacrylonitrile with a molecular weight of 100000 (PAN10), silicone-Polyhexamethylene adipamide (PA66), and silicone-Polytetrafluoroethylene (PTFE), respectively. The specific experimental preparation process can be found in the experimental section. Next, we selected 12 commonly used materials in daily life, such as aluminum (Al), polypropylene (PP), and polyvinyl chloride (PVC), as the recognition targets (the actual images of the 12 materials are shown in **Figure S13** (Supporting Information)). The V_{oc} of the three sensors in the FTS during the contact and separation process with the 12 different materials are shown in **Figure 5c**. It can be observed that different materials exhibit significant differences in both waveform and voltage magnitude, which preliminarily demonstrates that our sensor can successfully recognize different materials. To more clearly describe the differences in signal characteristics between the different materials, we evaluated them from multiple angles. First, we considered the sequence of the appearance of the signal peaks and troughs in the output voltage. For example, the waveform signals of Fluorinated ethylene propylene (FEP) and nylon are shown in the figure. The most significant difference between them is the sequence of the peaks

and troughs. For FTS, when the FTS contacts FEP, a trough appears first, followed by a peak after the sensor leaves the surface. Conversely, when the FTS contacts nylon, a peak appears first, followed by a trough upon separation. Additionally, the relative amplitude relationship of the three voltage signals can also be used for identification.

However, to extract more hidden features from the materials being identified and to enhance the accuracy of recognition, we introduced image recognition technology based on convolutional neural networks (CNN).^[17] Among them, ResNet50 is one of the representative networks of CNN.^[18] It builds upon the Alex Net model and further optimizes it by introducing residual connections to address the vanishing gradient problem in deep networks, allowing for the extraction of more abstract features when processing images. Due to its deeper network structure, the ResNet50 model possesses stronger learning capabilities for image feature extraction. Based on this, we modified the input layer and fully connected layer of the neural network model (ResNet50) and applied it to material identification. The entire process can be broadly divided into data acquisition, data preprocessing, model training, and material prediction. First, during the data acquisition process, we collected induced electrical signals by having a linear motor with predefined pressure and motion patterns contact different materials, resulting in the collection of output voltage signals from 12 different materials. Specifically, the total dataset used for the final training (containing 3600 sets) was derived from the V_{oc} outputs under different forces (0-0.5-1-1.5-2-2.5-3 N); the waveform of the three sensors in FTS contacting

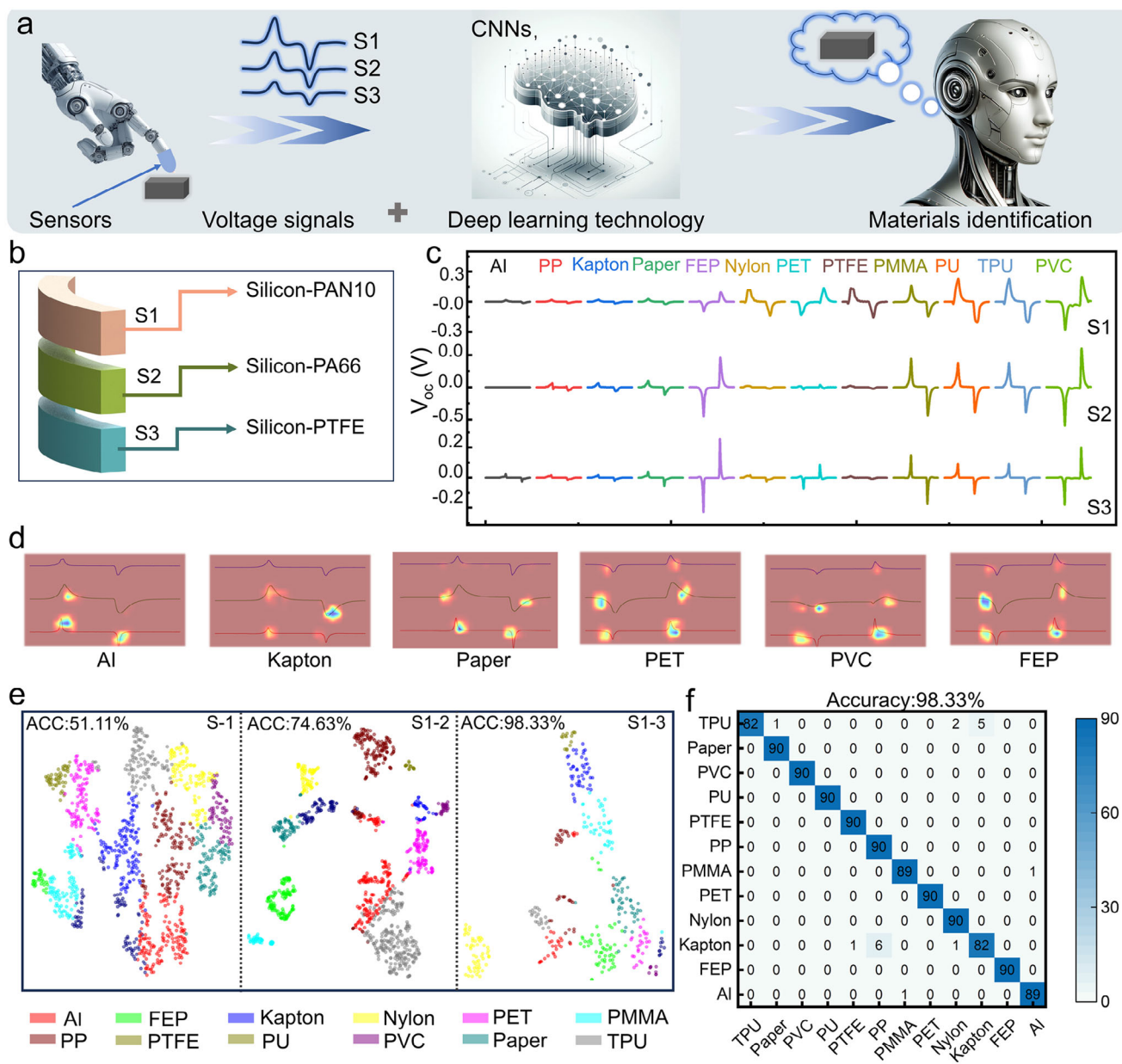


Figure 5. a) Schematic of the signal acquisition and data processing process. b) Schematic diagram of the material identification sensors in FTS. c) Waveform display of the FTS identifying 12 materials. d) Heatmap display of the FTS identifying six materials. e) Clustering diagram showing recognition accuracy with different numbers of sensors. f) Confusion matrix showing the accuracy of the FTS in identifying 12 materials.

FEP under different forces is shown in Figure S14 (Supporting Information)) and the conditions of the 12 materials.

After preprocessing the experimental data, we converted the three sets of normalized voltage data into images and performed uniform resizing and image enhancement. Through signal acquisition, the triboelectric signals from the three channels formed complete images. These images were normalized and then input into the ResNet50 model (with an input size of $517 \times 1092 \times 3$, where 517 and 1092 represent height and width, respectively, and 3 represents the number of channels) for classification of the 12 materials.

Subsequently, we preprocessed the data, trained, and made predictions using the model. The three sets of normalized voltage data were converted into images, which were then resized and enhanced before being processed by the ResNet50 model's own preprocessing functions and entered the model for training, validation, and testing. To better visualize the regions of the images that the model focuses on during the final classification decision, we employed Gradient-weighted class activation mapping (Grad-CAM) heatmap visualization on the output of the last "Bottleneck" module in the ResNet-50 model. As shown in Figure 5d, the heatmaps display the areas of focus for the model when it

touches six of the 12 materials under a pressure of 3 N; the remaining six materials are shown in Figure S15 (Supporting Information). In Grad-CAM heatmaps, colors are typically visualized from blue (low contribution) to red (high contribution), with red regions representing the areas the model considers most important for classification. The brighter the color (such as yellow and red regions), the stronger the model's activation in that area.

We further utilized the ResNet50 model to extract high-dimensional features from the data and visualized them using t-SNE and K-means algorithms to better understand and demonstrate the clustering effects of different materials. The goal of this approach is to minimize the distance between data points of the same class while maximizing the distance between the centers of different classes. As shown in Figure 5e, S_1 , $S_{1,2}$, and $S_{1,3}$ represent a series of data collected using one, two, and three material sensors, respectively, for training, validation, and testing. From the figure, when using data from a single channel, the clustering effect is poor, with the data distributed randomly, resulting in a classification accuracy of only 51.11%. However, as the number of channels increases (i.e., with more sensors), the clustering of the samples becomes more distinct and orderly. When using data from three channels, the clustering effect across multiple channels significantly improves, allowing for a clear distinction between different material types, and the classification accuracy increases to 98.33%. This demonstrates the significant advantage of multi-channel data in classification tasks, contributing to enhanced accuracy. The corresponding confusion matrix for the 12 materials is shown in Figure 5f (the confusion matrices for single and dual channels are provided in Figure S16 (Supporting Information)). In addition, to better highlight the performance characteristics of our device, we have compiled Table S1 for comparison (Supporting Information). It can be observed that the combination of the three triboelectric sensors in FTS and the ResNet50 model in this study achieved a high level of material identification accuracy.

2.3. Application of Multimodal Tactile Architecture in Intelligent Sorting

In the previous sections, we systematically demonstrated our FTS's capabilities in force sensing and material identification. To better illustrate the functionality of a tactile sensing system based on the integration of these two aspects in real-world scenarios, we integrated the device into the operating system of a robotic arm and hand, introducing a hybrid architecture that combines material identification and force sensing. As shown in Figure 6a, the process begins with the outermost material identification layer of the robotic hand's device encountering the material to be identified. The output features from the three recognition sensors in FTS are used as identification signals for different materials, which determine onto which conveyor belt the material should be placed on. Next, the internal force sensing component provides feedback on the gripping force when the robotic hand grasps the object, ensuring a successful grip. The object is then placed on the designated conveyor belt, completing the intelligent sorting process. As illustrated in Figure 6b and detailed video is shown in Video S4 (Supporting Information), we designed a real-time material identification program using LabVIEW software. The

general workflow is as follows: First, the robotic arm moves to a designated initial position (P_0) to prepare for operation. Then, as the robotic hand begins to bend and grasp, the V_{oc} data generated by the FTS during this process is extracted and saved as a "data" file. The LabVIEW program sends the address of this data file via TCP communication to the Jupyter-based material identification program. The material identification program locates and reads the data based on the address, processes it according to predefined preprocessing methods, and then feeds it into the pre-trained ResNet50 model for material identification. Subsequently, the server returns the preprocessed image address and material identification results to the LabVIEW program, which displays the preprocessed image and recognition results. This completes the entire material identification workflow, thereby enabling real-time data acquisition and material identification.

As a demonstration of the practical application, we selected three common packaging materials as test subjects: polypropylene (PP), polyvinyl chloride (PVC), and aluminum (Al). The operational scenario and real-time computer interface are shown in Figure 6c. When the robotic hand integrated with the FTS touches the test materials under appropriate conditions, the final prediction results are displayed on the right side of the computer screen, along with the corresponding conveyor belt number. The waveform diagrams of the FTS's response during the contact and separation of the three materials are shown in Figure 6d. Through this process, we successfully determined the material types and the corresponding conveyor belt numbers for transportation. Next, the identified object needs to be smoothly transported to the corresponding conveyor belt. We designed a flowchart, as shown in Figure S17 (Supporting Information), to guide this process. Specifically, the procedure begins with the robotic hand moving to the designated initial position P_1 , preparing for operation. Then, the hand enters state "N" and performs a bending action while the FTS starts collecting V_{oc} data. The normal force is calculated to determine if the FTS has made contact with the object to be grasped and to provide data for subsequent shear force calculations. Afterward, the robotic arm moves upward, and the FTS continues to collect V_{oc} data to calculate the shear force, assessing whether slide occurs during the operation. If the result indicates slippage ("yes"), the hand opens, moves back down to P_1 , enters state N+1, and repeats the bending and data collection steps. This loop continues until no slippage is detected ("no"), at which point the robotic arm moves the object to the designated conveyor belt for that material, preparing it for subsequent transport. The process ends here, with the robotic arm completing the assigned task.

The actual V_{oc} waveforms recorded during the gripping process are shown in Figure 6e. And the detailed video demonstration of this process is available as Video S5 (Supporting Information). Stage I represents the normal force detection, where the FTS's V_{oc} waveform indicates contact with the object and calculates the normal pressure for subsequent slide detection. Stage II involves shear force detection, where the robotic arm moves upward, and the FTS detects the V_o waveform indicating slippage. Stage III is the second normal force detection, where the robotic arm moves back down to P_1 , the hand opens, and then re-grips the object. The process then moves to Stage IV (the second tangential force detection), where the FTS does not detect the characteristic peak of slippage, indicating that the object has

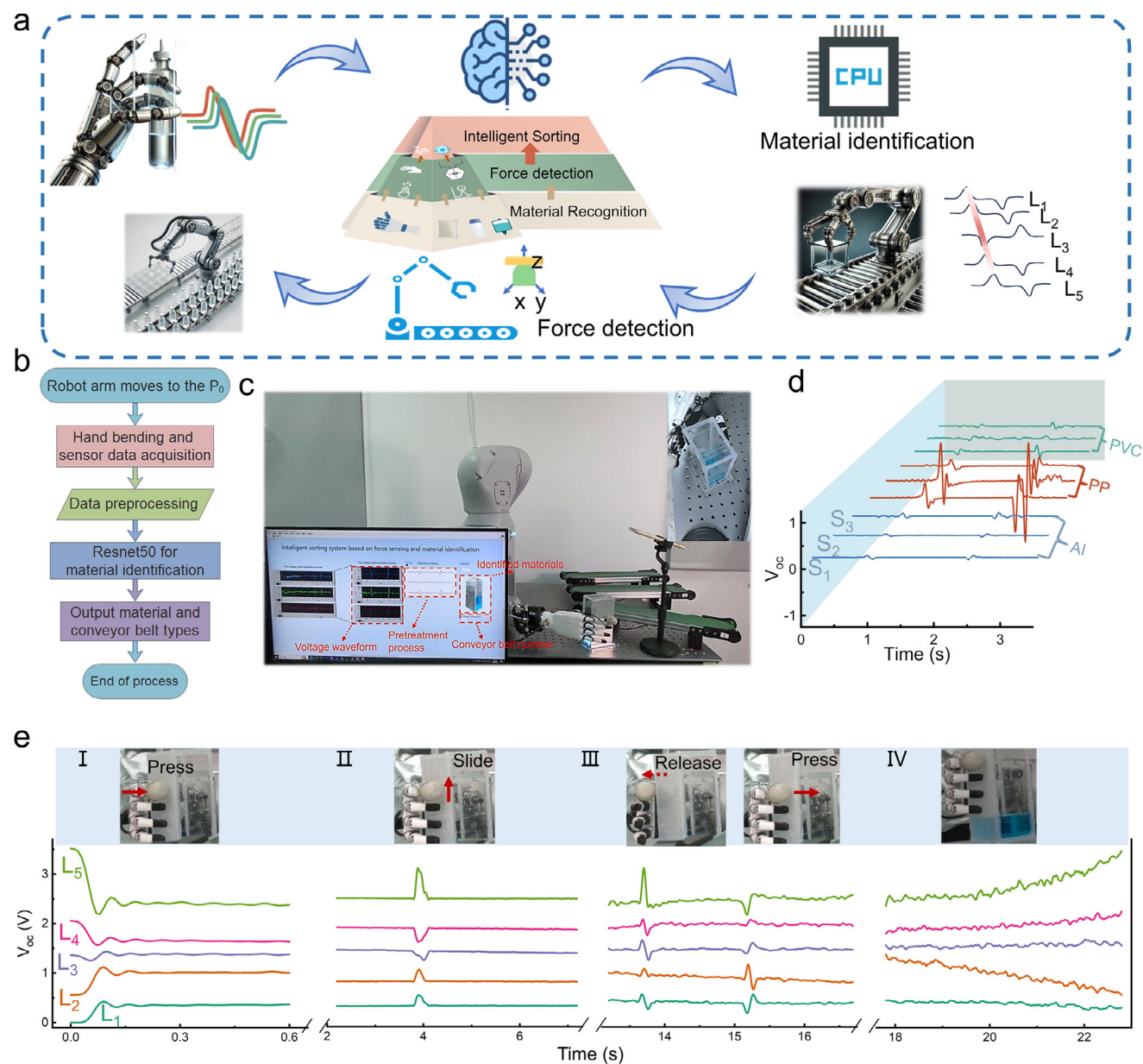


Figure 6. a) Hybrid architecture of tactile sensing based on intelligent analysis functions for material identification and force sensing. b) Flowchart of the material identification process. c) Scenario and computer interface display during the material identification process. d) Contact and separation waveforms of the FTS when identifying three different materials. e) Real-time output waveforms of the force sensor in FTS during object grasping: I. Normal force detection, II. Tangential force detection, III. Second normal force detection, IV. Second tangential force detection.

been successfully grasped. Finally, the robotic arm transports the grasped object to the corresponding conveyor belt, thus completing the entire intelligent sorting process. Crucially, the multimodal finger-shape tactile sensing system with multidirectional force and material detection might improve robot performance in challenging tasks by giving them richer and more precise sensing capabilities. As a result, it has significant applications in smart workshops, medical prosthetics, human–robot interaction. For more significant real-world applications, more test samples and sophisticated deep learning algorithms must be investigated in subsequent research.

3. Conclusion

In this study, we developed a finger-shaped tactile sensor (FTS) based on the triboelectric effect, capable of simultaneously detecting multidimensional forces and providing high-precision material identification. Inspired by the structure of the human finger, the sensor integrates an internal electrode with microneedles and bumps to accurately detect both normal and tangential forces. Experimental tests and simulations confirmed the sensor's stability and response under various force conditions. The material identification component, located at the finger pad, uses three

single-electrode triboelectric sensors made from different materials, achieving an accuracy of 98.33%. In practical applications, we integrated the FTS into a robotic hand and developed a real-time material identification system using LabVIEW and Jupyter, connected via TCP communication. This system successfully simulated real-time material identification and grip force detection in an intelligent workshop setting, transporting objects of different weights and materials to designated locations. This study demonstrates the potential of multimodal tactile sensing technology in intelligent robotics, particularly in force detection and material identification. The design and integration of the sensor provide valuable references for future applications in intelligent robotics and related fields.

4. Experimental Section

Preparation Process of the Force Sensor: In the material selection phase of the force sensor preparation: First, the mold for the microstructure was designed and then printed using a 3D printer. Next, different models of silicone (15#, 20#, 25#, 30#, 35#) were prepared, mixing the A and B components of each model in a 1:1 weight ratio. The mixture was then slowly poured into molds, ensuring no air bubbles were formed. The mixture was poured into pre-printed and cleaned molds and left to cure at room temperature for 6 h, ensuring complete curing of the silicone and achieving optimal mechanical properties. After curing, the required microstructure samples were carefully demolded. In the force sensor fabrication phase: First, the framework for the electrode part was printed using a 3D printer, with silver electrodes coated on the appropriate parts and wires attached at the corresponding positions. A three-part mold for the microneedle structure was also printed using 3D printing technology. The silicone rubber solution (Ecoflex 00–25) was prepared in a 1:1 ratio by volume and then poured into the mold, which was fixed and left to cure at room temperature for 3 h. Finally, after curing, the sample was treated in a vacuum plasma cleaner (Shanghai Zhongbin Technology Co., Ltd., CCI-PLA100) for 40 s, followed by applying a silver paste coating on the surface and attaching wires to serve as the shielding layer for the entire force sensor structure.

Preparation of the Material Identification Layer: Three portions of silicone rubber solution (Ecoflex 00–25) were prepared in a 1:1 ratio by volume. Three different polymer powders polyamide 66 (PA66, BASF SE), polytetrafluoroethylene (PTFE, DuPont USA), and polyacrylonitrile powder (PAN-10, Mw = 1000 000, Aladdin Chemical Co. Ltd.) were mixed into the silicone rubber solutions at a ratio of 8:1. The mixtures were thoroughly stirred and then poured into pre-printed molds, with conductive wires embedded before the silicone was fully cured. After curing, the samples were carefully demolded for later use. Next, the outermost silicone mold was printed. To achieve better integration, the previously prepared force-sensing components were placed in the center of the mold, and the silicone rubber solution was poured in, secured, and left to cure at room temperature for 3 h. Once fully cured, tweezers were used to carefully demold both sides of the mold. Finally, the three cured sensors for material identification were placed in their designated positions. With this, the fabrication of the FTS was completed.

Characterization and Measurement: The open-circuit voltage (V_{oc}) of the selected materials was measured using a programmable electrometer (Keithley 6514). For the basic output performance testing of the FTS and signal acquisition for the deep learning model, the programmable electrometer (Keithley Instruments 6514) was directly connected to a synchronous data acquisition card (National Instruments 6346) to simultaneously measure multi-channel voltage signals. A multi-channel data acquisition program developed on the LabVIEW platform was used to acquire, process, and store these data. The pressure sensor (SBT 674) was connected to a PC via a serial interface, allowing real-time display of pressure data from various measurement points. The data acquisition process was tested using a commercial linear motor (LinMot-E1200). In the robotic operating system application, the STM-32 chip was used to control and

collect V_{oc} data from each of the eight channels. These data were transmitted via SPI communication to a WIFI module, which then wirelessly transmitted the data to a mobile terminal, enabling real-time sensing and control within the LabVIEW interface. The multi-channel wireless signal acquisition circuit was developed and designed using Altium Designer, and the program code was written using MDK-ARM. A real-time material identification program was designed using TCP communication between LabVIEW and Jupyter.

Statistical Analysis: First, the data was processed using a LabVIEW program, which involved low-pass filtering (15 Hz) and segmenting the data into fixed-length segments. The data was then normalized using Python, standardizing the Y-axis voltage range. All voltage values were divided by the maximum value of the three voltage signals to ensure that all signals were compared on the same scale. The three sets of data were finally plotted on the same graph. Subsequently, the image size was adjusted to a fixed value (horizontal translation was applied during training), and then the images were further preprocessed using the ResNet50 model's built-in preprocessing method for subsequent training, validation, and testing. Next, a customized ResNet50 model was used, based on the classic architecture but adjusted to accommodate the classification task of 12 material categories. In ResNet50, the introduction of Residual Blocks effectively addresses the vanishing gradient problem in deep neural networks, enabling the training of deeper networks. The model loads a pre-trained ResNet50 and underwent two key modifications: first, the Adaptive Average Pooling layer (AdaptiveAvgPool2d) was replaced, reducing the output feature map size to 1×1 , allowing the model to flexibly handle input images of varying sizes; second, the fully connected layer was replaced, with the output feature count set to 12, tailored specifically for the classification task. During training, the model employed the Cross Entropy Loss function and the Adam optimizer, with an initial learning rate of 0.001. A learning rate scheduler (StepLR) was used to adjust the learning rate to 0.1 times the original value every 7 epochs. The training was conducted over 50 epoch, with a batch size of 4 during training and 1 during validation. The entire training process was conducted on a GPU (NVIDIA Quadro RTX 5000) to accelerate learning and ensure high-precision classification output.

Supporting Information

Supporting Information is available from the Wiley Online Library or from the author.

Acknowledgements

This work was supported by the National Key Research and Development Program of China (2023YFB3209400).

Conflict of Interest

The authors declare no conflict of interest.

Data Availability Statement

The data that support the findings of this study are available from the corresponding author upon reasonable request.

Keywords

deep learning, multi-dimensional force sensing, multimodal tactile sensing, real-time material identification, triboelectric nanogenerators

Received: September 18, 2024

Revised: December 11, 2024

Published online:

- [1] S. Chun, J.-S. Kim, Y. Yoo, Y. Choi, S. J. Jung, D. Jang, G. Lee, K.-I. Song, K. S. Nam, I. Youn, D. Son, C. Pang, Y. Jeong, H. Jung, Y.-J. Kim, B.-D. Choi, J. Kim, S.-P. Kim, W. Park, S. Park, *Nat. Electron.* **2021**, *4*, 429.
- [2] a) Z. Wang, N. Shi, Y. Zhang, N. Zheng, H. Li, Y. Jiao, J. Cheng, Y. Wang, X. Zhang, Y. Chen, Y. Chen, H. Wang, T. Xie, Y. Wang, Y. Ma, X. Gao, X. Feng, *Nat. Commun.* **2023**, *14*, 4213; b) I. You, D. G. Mackanic, N. Matsuhisa, J. Kang, J. Kwon, L. Beker, J. Mun, W. Suh, T. Y. Kim, J. B.-H. Tok, Z. Bao, U. Jeong, *Science* **2020**, *370*, 961; c) K. R. Jinkins, S. Li, H. Arafa, H. Jeong, Y. J. Lee, C. Wu, E. Campisi, X. Ni, D. Cho, Y. Huang, J. A. Rogers, *Sci. Adv.* **2022**, *8*, abo0537.
- [3] a) X. Zhang, L. Lu, W. Wang, N. Zhao, P. He, J. Liu, B. Yang, *ACS Appl. Mater. Interfaces* **2022**, *14*, 38409; b) B. Shih, D. Shah, J. Li, T. G. Thuruthel, Y.-L. Park, F. Iida, Z. Bao, R. Kramer-Bottiglio, M. T. Tolley, *Sci. Rob.* **2020**, *5*, aaz9239; c) D. Hoang, Y. Li, M. S. Jung, S. K. Sandstrom, A. M. Scida, H. Jiang, T. C. Gallagher, B. A. Pollard, R. Jensen, N.-C. Chiu, K. Stylianou, W. F. Stickle, P. A. Greaney, X. Ji, *Adv. Energy Mater.* **2023**, *13*, 2370173; d) Z. Song, J. Yin, Z. Wang, C. Lu, Z. Yang, Z. Zhao, Z. Lin, J. Wang, C. Wu, J. Cheng, Y. Dai, Y. Zi, S.-L. Huang, X. Chen, J. Song, G. Li, W. Ding, *Nano Energy* **2022**, *93*, 106798.
- [4] a) W. Lin, B. Wang, G. Peng, Y. Shan, H. Hu, Z. Yang, *Adv. Sci.* **2021**, *8*, 2002817; b) X. Fu, J. Zhang, J. Xiao, Y. Kang, L. Yu, C. Jiang, Y. Pan, H. Dong, S. Gao, Y. Wang, *Nanoscale* **2021**, *13*, 18780; c) E. Song, Z. Xie, W. Bai, H. Luan, B. Ji, X. Ning, Y. Xia, J. M. Baek, Y. Lee, R. Avila, H.-Y. Chen, J.-H. Kim, S. Madhvapathy, K. Yao, D. Li, J. Zhou, M. Han, S. M. Won, X. Zhang, D. J. Myers, Y. Mei, X. Guo, S. Xu, J.-K. Chang, X. Yu, Y. Huang, J. A. Rogers, *Nat. Biomed. Eng.* **2021**, *5*, 759.
- [5] a) Z. Sun, Z. Zhang, C. Lee, *Nat. Electron.* **2023**, *6*, 941; b) J. Lee, H. Sul, W. Lee, K. R. Pyun, I. Ha, D. Kim, H. Park, H. Eom, Y. Yoon, J. Jung, D. Lee, S. H. Ko, *Adv. Funct. Mater.* **2020**, *30*, 1909171; c) Y. Huang, J. Zhou, P. Ke, X. Guo, C. K. Yiu, K. Yao, S. Cai, D. Li, Y. Zhou, J. Li, T. H. Wong, Y. Liu, L. Li, Y. Gao, X. Huang, H. Li, J. Li, B. Zhang, Z. Chen, H. Zheng, X. Yang, H. Gao, Z. Zhao, X. Guo, E. Song, H. Wu, Z. Wang, Z. Xie, K. Zhu, X. Yu, *Nat. Electron.* **2023**, *6*, 1041.
- [6] a) K. K. Kim, M. Kim, K. Pyun, J. Kim, J. Min, S. Koh, S. E. Root, J. Kim, B.-N. T. Nguyen, Y. Nishio, S. Han, J. Choi, C. Y. Kim, J. B. H. Tok, S. Jo, S. H. Ko, Z. Bao, *Nat. Electron.* **2023**, *6*, 64; b) C. M. Boutry, M. Negre, M. Jorda, O. Vardoulis, A. Chortos, O. Khatib, Z. Bao, *Sci. Rob.* **2018**, *3*, aau6914.
- [7] C. Dhong, R. Miller, N. B. Root, S. Gupta, L. V. Kayser, C. W. Carpenter, K. J. Loh, V. S. Ramachandran, D. J. Lipomi, *Sci. Adv.* **2019**, *5*, aaw8845.
- [8] a) X. Wang, W.-Z. Song, M.-H. You, J. Zhang, M. Yu, Z. Fan, S. Ramakrishna, Y.-Z. Long, *ACS Nano* **2018**, *12*, 8588; b) B.-Y. Lee, D. H. Kim, J. Park, K.-I. Park, K. J. Lee, C. K. Jeong, *Sci. Technol. Adv. Mater.* **2019**, *20*, 758.
- [9] a) S. Mu, S. Li, H. Zhao, Z. Wang, X. Xiao, X. Xiao, Z. Lin, Z. Song, H. Tang, Q. Xu, D. Wang, W. W. Lee, C. Wu, W. Ding, *Nano Energy* **2023**, *116*, 108790; b) Z. Wang, J. An, J. Nie, J. Luo, J. Shao, T. Jiang, B. Chen, W. Tang, Z. L. Wang, *Adv. Mater.* **2020**, *32*, 2001466; c) C. Han, Z. Cao, Y. Hu, Z. Zhang, C. Li, Z. L. Wang, Z. Wu, *Nano Lett.* **2024**, *24*, 5277; d) Z. An, Z. Wu, Y. Hu, C. Han, Z. Cao, H. Zhou, Y. Chen, *Nano Energy* **2024**, *125*, 109567.
- [10] H. Yamazaki, M. Nishiyama, K. Watanabe, *IEEE Sens. J.* **2017**, *17*, 5123.
- [11] Y. Xu, S. Zhang, S. Li, Z. Wu, Y. Li, Z. Li, X. Chen, C. Shi, P. Chen, P. Zhang, M. D. Dickey, B. Su, *npj Flexible Electron.* **2024**, *8*, 2.
- [12] H. Sun, K. J. Kuchenbecker, G. Martius, *Nat. Mach. Intell.* **2022**, *4*, 135.
- [13] T. P. Tomo, A. Schmitz, W. K. Wong, H. Kristanto, S. Somlor, J. Hwang, L. Jamone, S. Sugano, *IEEE Rob. Autom. Lett.* **2018**, *3*, 124.
- [14] a) L. Zhao, H. Li, J. Meng, A. C. Wang, P. Tan, Y. Zou, Z. Yuan, J. Lu, C. Pan, Y. Fan, Y. Zhang, Y. Zhang, Z. L. Wang, Z. Li, *Adv. Funct. Mater.* **2020**, *30*, 1907999; b) X. Wei, B. Wang, Z. Wu, Z. L. Wang, *Adv. Mater.* **2022**, *34*, 2203073.
- [15] X. Zhao, Z. Sun, C. Lee, *Adv. Funct. Mater.* **2024**, *34*, 2409558.
- [16] a) W. He, W. Liu, J. Chen, Z. Wang, Y. Liu, X. Pu, H. Yang, Q. Tang, H. Yang, H. Guo, C. Hu, *Nat. Commun.* **2020**, *11*, 4277; b) S. An, S. Fu, W. He, G. Li, P. Xing, Y. Du, J. Wang, S. Zhou, X. Pu, C. Hu, *Small* **2023**, *19*, 2303277.
- [17] a) Y. Xu, H. Zhang, *Neural Networks* **2022**, *153*, 553; b) S. Mohsen, A. M. Ali, A. Emam, *Multimedia Tools Appl.* **2024**, *83*, 7035.
- [18] L. Zhang, H. Schaeffer, *J. Math. Imaging Vision* **2020**, *62*, 328.